

Modelling Irradiation Induced Processes in Metal Organic Frameworks

James Pierce

School of Chemistry, University of Nottingham, NG7 2RD UK

Submitted: 13th May 2022

Abstract

Ab initio molecular dynamics simulations were employed to study the stability of two copper based metal organic frameworks during transmission electron microscopy. Irradiation induced elastic scattering events were simulated to study knock-on damage causing atomic ejection. It was shown that atom types present played a key role in determining the resilience of metal organic frameworks to knock-on effects, due to their influence on direct electronic energy transfer. However, it is unlikely that this is the only effect of importance, and it is theorised that other factors such as electronic conductivity are likely to play a role in resilience.

1. Introduction

Metal organic frameworks (MOFs) are crystalline porous materials made by connecting inorganic metal ions to organic ligands.¹ This is achieved by coordination, which leads to the open framework that MOFs enjoy. They often demonstrate permanent porosity due to their long organic linkers, which provide large open pores within the MOF structure. These pores act as large storage spaces that contain numerous adsorption sites within MOFs.² There are a large variety of MOF structures attainable due to the range of coordination geometries of the metal ion centres, as well as the range of possible organic linkers. This allows MOF structures to be tailored to purpose,³ and can be seen in the literature with the array of 1-, 2-, and 3-D MOFs that have been identified.⁴

These compounds have been of high interest in recent years, as can be seen with more than 20,000 different MOFs having appeared in the literature in the past decade.⁵ This is in large part due to their desirable properties such as permanent porosity, open framework, high surface area, and pore vol-

ume, which give MOFs their commercial appeal.^{2,4,6,7} These properties are what has led to the diversity in areas of research in which MOFs are now being applied, ranging from gas adsorption and storage, drug delivery, antimicrobial properties, medical imaging and luminescence applications.^{2,5,8,9}

However, MOFs in general suffer from a lack of stability, and are particularly susceptible to thermal decomposition,¹⁰ desolvation collapse,¹¹ and dissociation during imaging.¹² The stability of a MOF is primarily determined by its metal-ligand coordination bond strength.¹³⁻¹⁵ This strength is dependent on the metal ion within the MOF, and the functionalities present within the ligand.

While there are no systematic studies comparing MOF functionalities to electron beam resilience, Wiktor *et al.*¹² state that the metal centre of a MOF is crucial in determining its electron beam stability, with Cu and Ru ions in MOFs frequently being reduced by the beam to form nanoparticles within the MOF matrix. They further go on to say that the organic linkers have less of an effect, however, the lighter atoms that they

introduce can be completely removed by inelastic scattering, leaving highly reactive species.

This work aims to address this gap within the literature by providing a better understanding of the processes that cause fragment ejections from MOFs during transmission electron microscopy (TEM). Subsequently, the focus has been on MOF behaviours that arise at beam energies of around 300 keV, as this is where fragment ejection becomes the predominant process.^{16,17}

In partnership with experimental collaborators (U. Kaiser.; H. Qi, 2021, private communication, 19th January)¹⁸ an array of MOFs were chosen to be studied. These MOFs are $\text{Cu}_3(\text{Hexaiminobezene})_2$, $\text{Cu}_3(\text{Hexahydroxybenzene})_2$, $\text{Cu}_3(\text{Hexahydroxybenzene})$, and $\text{Cu}_3(\text{Benzenehexathiol})$, and shall be denoted as HAB, HHB-2, HHB-1, and BHT respectively, and can be seen in Figure 1

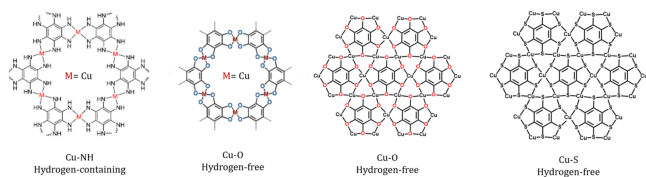


Figure 1. The array of MOFs being studied in partnership with experimental collaborators.

2. Theory

During TEM, a beam of electrons is fired at a thin layer of the sample being studied. As electrons move through said sample, they experience an electrostatic attraction between themselves and the nuclei of the layer. The force experienced is inversely proportional to the square of the radius,¹⁹ and so electrons that travel along paths closer to the nuclei experience a greater attraction. When this attraction causes an electron to deviate from the original beam direction and travel along an alternate path, this is known as scattering. Every scattering event is associated with a scattering angle

θ , which is defined as the angle between the original electron beam direction and the new electron direction of travel, as can be seen in Figure 2. Should an electron travel close enough, the force experienced may be sufficient to cause a total reversal in the direction of travel. This is known as back scattering.

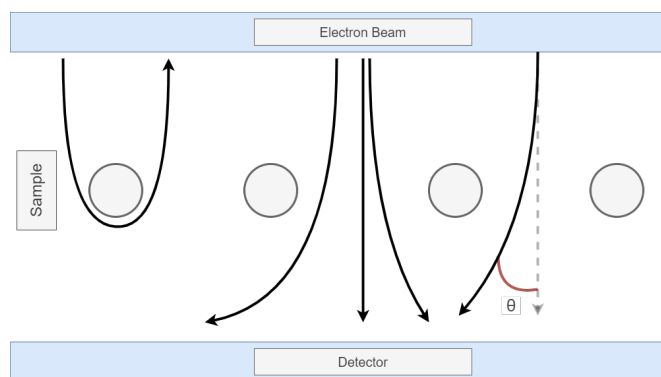


Figure 2. The electron interactions during transmission electron microscopy.

The signals produced from the electrons reaching the detector are used to generate an image. Bright spots result from regions with a high density of electron impacts, whereas dark spots are from the absence of electron detection. This generates an image with dark regions corresponding to the position of nuclei that caused electron scattering, and results in an image of the nuclear positions of the sample being studied.

TEM techniques are now being used to obtain a structural understanding of MOFs, as they offer atomic scale resolutions which provide the most detailed images for analysis.^{20–22} However, TEM hasn't yet reached large scale success with regards to MOF imaging as the electron beams used are of considerably high energy, which can be transferred to the MOFs being imaged and cause fragmentation, and ultimately complete structural decomposition.^{23,24} This damage can be seen in the electron diffraction pattern of the imaged sample, where the peaks of electron intensity fade or become blurred as the regular atomic arrangement is disrupted.²⁵ Techniques have been developed to overcome this issue such as reducing

the beam energy or dose rate, but they are expensive and not widely available.^{26,27}

There are two mechanisms by which electrons are scattered by atoms, elastic scattering and inelastic scattering.²⁸ Both mechanisms contribute to the overall sample degradation during TEM imaging.²⁹ This research specifically focuses on elastic scattering with it being the major process with regards to fragment ejection at 300 keV beam energies. As such from this point forward, all scattering events are considered to be elastic.

Elastic scattering transfers energy from an electron to a nucleus equal to

$$E = E_{\max} \cdot \sin^2 \left(\frac{\theta}{2} \right) \quad (1)$$

where θ is the scattering angle and E_{\max} is the energy loss for 180° scattering.²⁵ Most elastic scattering involves angles below 1°, corresponding to an electron energy loss of about 1 eV²⁵. This low angle scattering is responsible for the electron diffraction pattern observed in TEM. However, the small fraction of electrons that scatter through large angles experience a considerable energy loss. This can cause the corresponding nucleus to eject from the sample if the energy delivered exceeds a threshold energy E_d , the ejection energy threshold. This process removes atoms from the imaged sample, and can lead to a loss of structural order or a complete decomposition of the sample, causing information to be lost from the observed diffraction pattern.^{25,30}

In order to measure stability a metric known as cross section is commonly used. Cross section is proportional to the probability that a species dissociates from the sample being imaged, and is measured in barn, or 10^{-28} m^2 . It is calculated

using the formula:

$$\sigma_d = 4\pi \left(\frac{z \cdot e^2}{4\pi\epsilon_0 \cdot 2m_e c^2} \right)^2 \cdot \frac{1 - \beta^2}{\beta} \left\{ \frac{T_{\max}}{E_d} - 1 - \beta^2 \cdot \ln \left(\frac{T_{\max}}{E_d} \right) + \pi \frac{z \cdot e^2}{\hbar \cdot c} \beta \left[2 \left(\frac{T_{\max}}{E_d} \right)^{\frac{1}{2}} - \ln \left(\frac{T_{\max}}{E_d} \right) - 2 \right] \right\} \quad (2)$$

where z is the nuclear charge, $\beta = \frac{v_e}{c}$ is the ratio of electron velocity v_e to the speed of light, c , m_e is the mass of an electron and T_{\max} is the maximum kinetic energy that an electron can confer to an atom.³¹ It is calculated by:

$$T_{\max} = \frac{2ME \cdot (E + m_e c^2)}{(M + m_e)^2 + 2ME} \quad (3)$$

where M is the mass of the atom, and E is the electron kinetic energy.³² This equation for T_{\max} applies to stationary atoms. An alternative approach that considers the affect of velocity distributions on T_{\max} is:

$$T_{\max} = \frac{1}{2M} \left(r \left(r + \frac{2t}{c} \right) + \left(\frac{t}{c} \right)^2 \right) \quad (4)$$

$$r = \frac{1}{c} \sqrt{E(E + 2mc^2)} + MV_n \quad (5)$$

$$t = \sqrt{(E + E_n)(E + 2mc^2 + E_n)} \quad (6)$$

where V_n is the initial velocity distribution at a given temperature of the atoms parallel to the electron beam and E_n is the initial kinetic energy of the atom.³³

The term E_d in Eq.(2) is the ejection energy threshold. It is the minimum energy that the atom requires to dissociate and must be obtained analytically through computational methods. E_d captures the bond strength between the atom and the total imaged species, and is therefore greater for more stable species. If T_{\max} is less than E_d then there isn't sufficient energy to break the bonds and no dissociation takes place. However, if T_{\max} is greater than E_d then dissociation of the

atom is possible.²⁵ The probability that the atom rejoins the molecule is dependent on its kinetic energy after dissociation and so cross section, σ_d , is dependent on a combination of these two terms.

Experimentally, a metric known as critical dose can be obtained which is also proportional to, and a measure of, stability. It is defined as the number of electrons needed to degrade a sample to the point where a diffraction pattern is no longer observed.

3. Methodology

As previously stated, the ejection energy threshold must be obtained analytically through computational methods. After reviewing the literature, it was found that both *ab initio* molecular dynamics (AIMD), as well as empirical potential methods have been used to study electron irradiation induced processes before, however neither has been applied to study the dynamics during MOF irradiation. Classical potentials are ideal for nonreactive interactions such as angle-strain, dispersion, and coulombic interactions, but often fail to capture changes in atomic connectivity. There have been more recent approaches that attempt to overcome this by including a bond-order formalism into potentials, allowing them to capture reaction chemistry more accurately, however direct quantum calculations offer the most accurate picture, although with the added computational cost. As the primary focus of study is with regard to atomic connectivity, it was decided that the increased accuracy that AIMD would provide was beneficial.

The MOF coordinates were taken from cif files, as seen in Figure 1. These structures were far too large and would make the *ab initio* techniques too expensive to perform, so a reduced fragment of each MOF that was representative of the extended system was used in all calculations. These representative frag-

ments are shown in Figure 3. The reduced fragments were ideal as they contained the key functionalities present in each MOF, but greatly reduced the computational complexity.

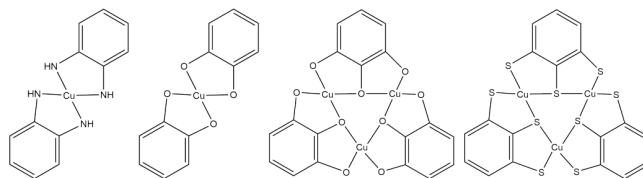


Figure 3. The array of MOF reduced structures to be used in simulations.

In order to keep the fragments representative of the extended MOF system, outer atoms needed to be frozen, to set a boundary on the allowed movement that the fragments could take. Because of this, the ORCA³⁴ software package was used to run the simulations, as it provides better tools to exclude atoms from simulations when compared to other packages.

During a molecular dynamics simulation the energy is calculated at each timestep. As we have chosen to use an *ab initio* approach, this is calculated using density functional theory (DFT).³⁵ Within the DFT procedure, the energy of the electrons need to be converged. This is achieved by the use of the self consistent field method (SCF), which aims to minimise the energy, gradient, and forces, converging them to zero in an iterative process. Second order SCF (SOSCF) is also used in some cases to improve convergence, but in other situations it can in fact be detrimental. Trial and error must be employed to find which approach is preferential to each simulation. ORCA requires an SOSCF threshold to be provided, which determines when each technique is deployed to achieve convergence. Further to this, we chose to use the B3LYP method and 6-31G* basis set as this setup is general and widely applicable, seeing a broad usage within the literature. There was an interest into whether other basis sets would fare better at capturing the chemistry of the Cu centres, as seen with sets such as the 6-31+G** + LANL2DZ mixed

basis set.³⁶ However, the widely applicable 6-31G* basis set was chosen as it provides a reasonable accuracy and is less computationally expensive.

3.1 Simulation Setup

To run AIMD simulation using the ORCA package, we first generated a restart file, named .mdrestart, which allows the specification of forces and velocities that each atom experiences. This is generated using an input file running for one timestep that contains the initial coordinates. The .mdrestart file generated contains the initial coordinates, velocities, and forces that each atom experiences. Each force value is then set to zero, as well as each velocity value, except the value that corresponds to the atom being simulated for irradiation, the principle knock-on atom (PKA).

The velocity value for this atom is set to the maximum velocity transferred to the atom due to irradiation from the specific beam energy. This is obtained from taking the maximum value of equation 3, which is when the electron kinetic energy is at its maximum. This is obtained by maximizing equation 1, when the scattering angle θ is at its maximum, 180° .

Once the mdrestart file has been adjusted correctly it can be used in combination with an input file to carry out the AIMD simulation for a specified amount of time steps, with a provided convergence criteria and iteration limit.

4. Results

It was known that the ejection energy threshold for carbon in HHB-2 was equivalent to a beam energy of around 97 keV, and this guided the selection of a suitable testing range when starting the initial simulations. Consequently, a range of beam energies were simulated on each atom type from both MOFs over a range of 50 keV to 100 keV in 5 keV increments. For all simulations the SOSCF implementation value was chosen

to be 0.00003, with a max iteration value of 500, and each simulation was run for 600 time steps with each time step corresponding to 0.5 fs. These simulations had also had a maximum run time of 12 hours.

As seen in Figure 4, for all simulations, atoms 2, 3, 22, 23, 29, 31, 33, and 34 were frozen in all HHB-1 simulations, and atoms 5, 6, 24, 25, 28, 31, 32, and 39 were frozen for all BHT simulations. In addition, for HHB-1 all carbon, oxygen, and copper irradiations were simulated on atoms 12, 25, and 11 respectively, and for BHT all carbon, oxygen, and copper irradiations were simulated on atoms 28, 30, and 11 respectively.

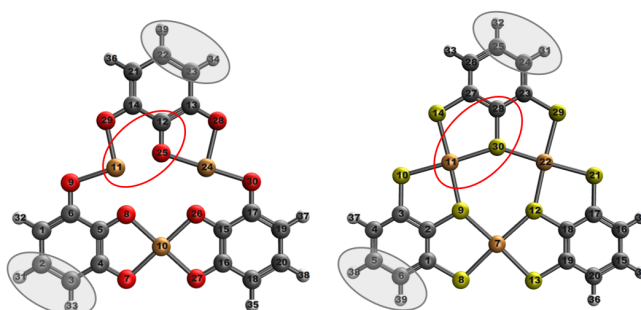


Figure 4. MOF structures with frozen atoms circled in grey, and irradiation atoms circled in red. HHB-1 on the left, BHT on the right.

With regards to HHB-1, the results of the initial simulations placed an upper bound for the ejection energy threshold of carbon at 100 keV and a lower bound at 55 keV. This large range was due to the simulations being terminated after 12 hours, and as such none were able to complete the full 600 timesteps. Subsequently, all of the simulations within the specified range had not settled into a stable end point, and so were inconclusive. Of the other simulations conducted, the initial bound for oxygen was found to be between 70 keV and 85 keV, and the bound for copper was found to be greater than 150 keV. When reviewing the oxygen simulations, it was found that the oxygen atom was reliably ejected above 110 keV, however between the upper ejection bound of 85 keV and this value it was surprisingly a carbon monoxide fragment

that was ejected. This remained a consistent feature of all future simulations and demonstrates an interesting feature that it can be energetically favourable for a molecule to be ejected instead of atomic species. Simulations of BHT placed the ejection energy threshold between 85 keV and 110 keV for carbon, greater than 140 keV for sulphur, and greater than 150 keV for copper.

As previously stated, the first round of simulations were terminated prematurely. This led us to extend the termination time to 24 hours for the second round and so some energies were repeated to see whether the system could settle into a stable end point with the added simulation time. As such, for HHB-1, carbon was investigated over the range of 50 keV to 100 keV, oxygen over 60 keV to 120 keV, and Cu over 145 keV to 200 keV, all with increments of 5 keV. The same ranges were applied to carbon and copper in BHT, however sulphur was studied over the range 145 keV to 200 keV. For these simulations it was found that the ranges for carbon, oxygen and copper in HHB-1 were 85 - 100 keV, 70 - 90 keV, and greater than 200 keV respectively. For BHT the ranges for carbon, sulphur, and copper were found to be 85 - 100 keV, 155 - 170 keV, and greater than 200 keV respectively. These simulations improved upon the previous ranges, however most simulations were not reaching a stable end point after 1200 timesteps, and there were issues with convergence, especially for the copper simulations.

In response to the issues that arose, the SOSCF threshold was removed and the maximum iterations was increased to 800 for all further copper simulations. Furthermore, all simulations were extended to 1200 timesteps and the termination time was increased to 36 hours. The carbon, oxygen, and copper atoms of HHB-1 were tested over the ranges 85 - 100 keV, 70 - 90 keV, and 225 - 270 keV respectively, all with 5 keV increments. These simulations placed the carbon ejection

energy threshold between 90 keV and 95 keV, the oxygen threshold between 75 keV and 80 keV, and the carbon threshold between 260 keV and 275 keV. BHT's carbon, sulphur and copper atoms were tested over the ranges 85 - 100 keV, 155 - 170 keV, and 225 - 270 keV respectively, all with 5 keV increments. These simulations placed the carbon ejection energy threshold between 95 keV and 100 keV, the sulphur threshold between 160 keV and 165 keV, and the carbon threshold between 260 keV and 275 keV.

Table 1. Ejection energy thresholds obtained for each atom type in each MOF

PKA	Ejected Atom(S)	Beam Energy (keV)	Transferred Energy (eV)
HHB-1			
C	C	90 - 95	17.905 - 18.984
O	CO	79.0 - 79.5	11.671 - 11.750
Cu	Cu	260 - 265	11.360 - 11.623
BHT			
C	C	95 - 100	18.984 - 20.073
S	S	164.5 - 165.0	13.095 - 13.141
Cu	Cu	260 - 265	11.360 - 11.623

Due to time constraints certain simulations had to take priority over others. It was decided that the thresholds for oxygen and sulphur were of particular interest, due to them being the distinct atoms in each MOF. As such for the final round of simulations, oxygen was tested over the range 75.5 - 79.5 keV, and sulphur was tested over the range 160.5 - 164.5 keV, with both ranges dividing in 0.5 keV increments. These simulations then provided us the bounds of 79.0 - 79.5 keV for oxygen, and 164.5 - 165.0 for sulphur. Copper was the next atom of interest as its range had not been reduced down as far as the other atoms. Due to this, copper in HHB-1 was simulated over 260 - 275 keV in 5 keV increments, and placed the threshold between 260 - 265 keV. Copper in BHT was simulated over 260 - 275 keV in 5 keV, and the threshold was found to be between 260 - 265 keV.

To summarise, Table 1 shows the final ejection energy thresh-

old upper and lower bound that was found for the atoms in each MOF. Having obtained ejection energy thresholds for each atom, it was then possible to use equation 2 to calculate cross section values.

As the ejection energy thresholds obtained were over a range of values, cross section values were found for thresholds at different points within each range. Specifically, the minimum, median, and maximum in each range for the ejection energy threshold were used to find cross section values over a range of beam energies, and are shown in Figure S7. It can be seen that there is minimal variation in the cross sections of each atom for each ejection threshold value, and so the median value could be confidently used for all further calculations. These atomic cross sections for each MOF can be seen in Figure 5.

It can be seen that there is minimal variation in the carbon cross sections shown in Figure 5a and Figure 5b, as well as the copper cross sections. Both oxygen in Figure 5a and sulphur in Figure 5b have noticeable difference in behaviour compared to each other. At lower energies, sulphur displays a greater stability than oxygen, however above 322 keV sulphur starts to have a cross section that is greater than that of oxygen, and so is less stable.

The atomic cross sections were then used to calculate the total cross section for each MOF. There are different approaches to calculate the cross section, and each can be seen in equations 7, 8, and 9. Values used within these calculations can be found in Table S5 in the supplementary information.

Total Cross Section:

Per Cu =

$$\sum N_{\text{Atoms per Cu}} \times \sigma_{\text{Atom}} \quad (7)$$

Per Equivalent Cu in HHB-2 =

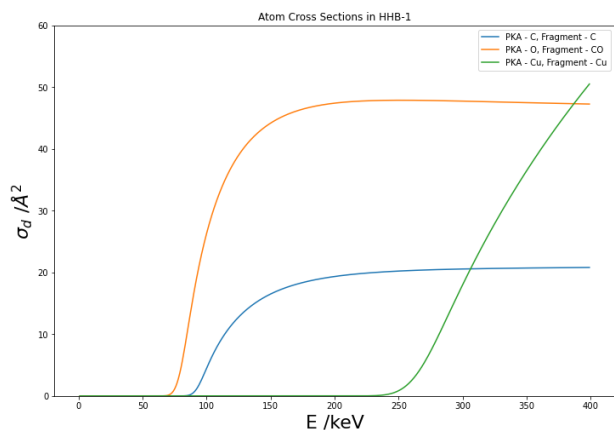
$$\sum N_{\text{Atoms per equivalent Cu in HHB-2}} \times \sigma_{\text{Atom}} \quad (8)$$

Per Area =

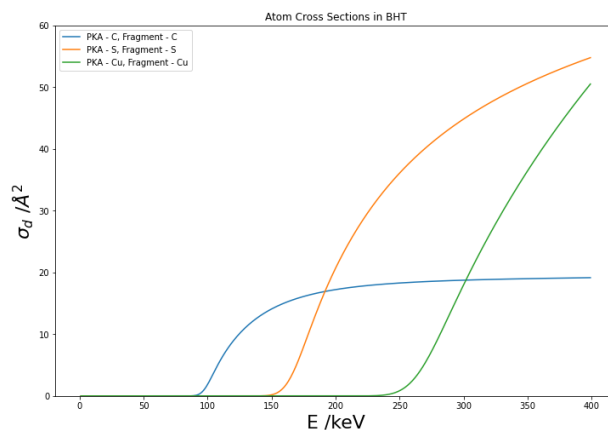
$$\sum N_{\text{Atoms per Area}} \times \sigma_{\text{Atom}} \quad (9)$$

Plots comparing the different total cross section approaches can be seen for each MOF in Figure 6. As seen in Figure 6a and 6b, both approaches capture the characteristic trend of the cross section of each MOF, with a scaling factor influencing the absolute value due to differences in density of these MOFs with the HHB-2 standardisation. For these MOFs, this density consideration only has a scaling effect as both MOFs have the same ratio of atoms to copper. Figure 6a and 6b show that at lower energies BHT is more stable than HHB-1, however at higher energies it is in fact HHB-1 that is more stable than BHT. In contrast, Figure 6c exhibits a different behaviour in the cross section curve for each MOF. This graph shows that at all energies BHT is more stable than HHB-1. This arises due to the bond length between copper and sulphur being greater than the bond length between copper and oxygen, which causes BHT to be spread over a larger area than HHB-1. This leads to a reduced likelihood of electron irradiation events as electrons are more likely to be fully transmitted through the MOF, due to the increased empty space, resulting in a lower cross section per area, and therefore a greater stability.

The total cross section values for each MOF within the array being studied can be seen in Figure S8 and the values at 300 keV were then compared. These values can be seen in



(a) Atom Cross Sections of HHB-1



(b) Atom Cross Sections of BHT

Figure 5. Atom Cross Sections of HHB-1 and BHT

Table 2. From this table we can see that comparing the total cross section per Cu, HHB-2 is twice as stable as HAB, HHB-1 is twice as stable as HHB-2, and BHT is slightly more stable than HHB-1. However, comparing the total cross section per equivalent Cu in HHB-2, we can see that HHB-2 is still twice as stable as HAB, however now HHB-2 is also twice as stable as HHB-1, which is still slightly less stable than BHT. Finally, the total cross section per area shows that HHB-2 is around one-and-a-half times more stable than HAB, HAB is slightly more stable than HHB-1, and BHT is one-and-a-half times more stable than HHB-1.

Table 2. MOF Total Cross Section values

Total Cross Section at 300 keV	HAB	HHB-2	HHB-1	BHT
per Cu (barn)	470.75	286.77	154.658	145.26
per equivalent Cu in HHB-2 (barn)	470.75	286.77	463.975	435.781
per area (\AA^2)	8.95	5.79	9.52448	6.64813

Each metric considers different factors when evaluating the total cross section for each MOF, and so it is not necessarily obvious as to which approach is the most reasonable. To provide some insight we compared these values with the experimental results obtained by the collaborators. Their critical dose values for each MOF can be seen in Table 3.

From this table it can be seen that experimentally HHB-2 is

Table 3. MOF critical dose values¹⁸

MOF	Critical dose ($\text{e}^- \text{\AA}^{-2}$)
HAB	$(4.45 \pm 0.31) \times 10^3$
HHB-2	$(7.80 \pm 0.89) \times 10^3$
HHB-1	$(8.91 \pm 0.41) \times 10^3$
BHT	$(3.13 \pm 0.39) \times 10^5$

twice as stable as HAB, HHB-1 has around the same stability as HHB-2, and BHT is two orders of magnitude more stable than HHB-1. Looking back at Table 2, we can see that no one approach on its own captures the correct picture entirely. Total cross section per Cu is the only metric that captures the similarity in stability of HHB-1 and HHB-2, and cross section per areas is the only one that successfully displays an increase in stability from HHB-1 to BHT. The most important observation is that not a single approach manages to capture the orders of magnitude increase in stability that BHT enjoys compared to all other MOFs. From comparing computational and experimental results, it is now believed that there are other factors at play that are not included in the simulations.

Table 4. MOF electronic conductivity: HAB³⁷, HHB-2³⁸, HHB-1¹⁸ and BHT³⁹

MOF	Electronic conductivity at 298 K
HAB	13 S cm^2
HHB-2	$7.3 \times 10^{-8} \text{ S cm}^2$
HHB-1	$2.6 \times 10^{-2} \text{ S cm}^2$
BHT	2500 S cm^2

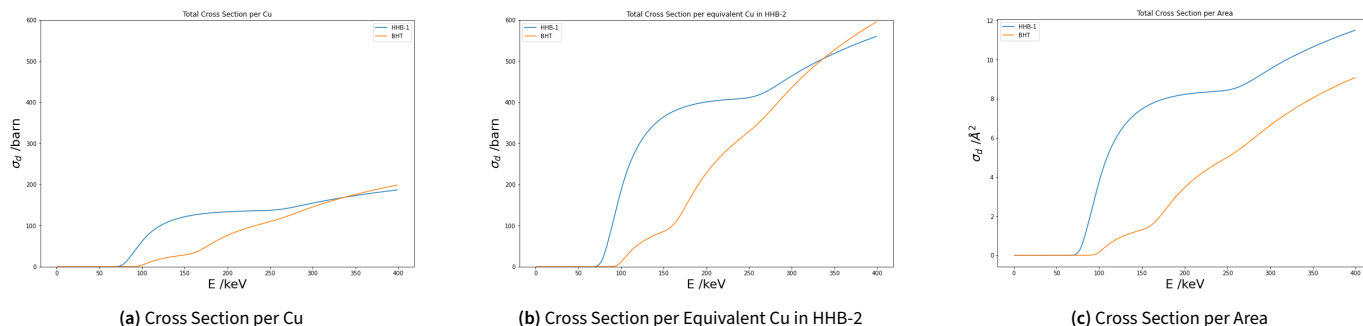


Figure 6. Total Cross Sections of HHB-1 and BHT

When reviewing the properties of each MOF it was observed that the electrical conductivity of BHT was orders of magnitude greater than that of the other MOFs, as seen in Table 4. It is believed that an increased electrical conductivity would increase a MOFs stability by decreasing the likelihood of ejection events. This is because the knock-on effects causing ejections could be dampened as the MOF would have a greater ability to diffuse charge density, and so be more resilient to perturbations, resulting in a drive back towards the original stable structure, and a reduced probability of ejection. Once a fragment has been ejected from the MOF leaving a radical, this effect would also allow for the charge to be diffused and help to stabilise the resulting MOF species, reducing the likelihood of further decomposition, compared to an unstable species which would be more vulnerable to such irradiation events. Electrical conductivity is a property that comes from an extended structure that allows for charge delocalisation, and would be present in the large MOF fragments used in experiments. In comparison, our model uses a reduced structure of the MOF due to computational constraints. This greatly reduced structure would not accurately capture electrical conductivity, and this would explain why the MOF that would be the most affected by this, BHT, has had the least success when modelling its stability. It is now believed that electrical conductivity, as well as knock-on effects play an important role in atomic ejection.

Another issue under consideration is that the model only captures an atom-thick layer of the MOF. In practise, samples imaged using TEM can be multi-layered extensive sheets. These layers can all interact with the beam and experience atomic ejections, which can impact other layers, leading to further ejections. Secondary electron ejections from layers can also interact with further layers, leading to atomic ejections. To model such a system it would be sensible to use a classical potential which would make more complex systems computationally accessible. However, this would come with a reduced accuracy and as stated previously, such potentials are known to suffer at capturing atomic connectivity, and so data obtained would be less reliable. After discussions with collaborators, the thickness of their studied MOFs has yet to be determined, but is known to be of low dimension. This gives us reassurance that the fragments that we have modelled are reasonable in capturing the effects due to thickness, however they are not going to be exact. The uncertainty that this thickness ambiguity introduces could provide an explanation for the disconnect between theory and experiment, as these thickness dependent processes could be having more of an effect on experimental results than is currently assumed.

It was already known that groups such as hydrogen can play a key role in sample degradation for compounds such as coronene during TEM, however it was not known whether this would translate to the field of MOF TEM. This work has re-

vealed that some atoms are more susceptible to the electron beam, and cause more expedient sample degradation than others. Oxygen and sulphur display a larger influence on the stability of the studied MOFs, HHB-1 and BHT, with sulphur allowing for stabilisation due to electrical conductivity. This must arise due to the fact that sulphur has a much greater mass, and as such has less energy transferred to it by an electron at a given beam energy, leading to a lower probability of ejection. Sulphur also has more p orbitals allowing for a greater participation in π systems, as well as having outer p orbitals providing a better interaction with copper's p and d orbitals, leading to a far better delocalised system for the MOF.

5. Conclusion

Overall, this work has shown that ligand functionalities greatly influence the stability of MOFs, with heavier and larger atoms such as sulphur having a stabilising influence, whereas comparatively smaller atoms such as oxygen have the effect of increasing the capacity for degradation at 300 keV. However, more work is needed to understand the effect that other macroscopic properties such as electronic conductivity, which are not captured in this approach, have on MOF stability.

Acknowledgements

Many thanks to Dr Elena Besley, Isabel Cooley, Rachel Heelas, the Besley group, the Kaiser group, and the Feng group.

References

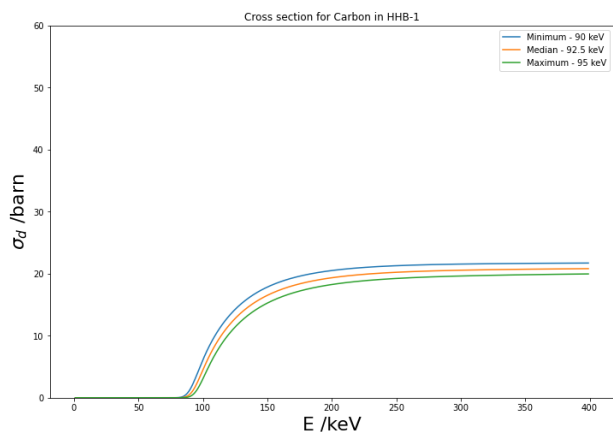
- [1] M. Zhao, Q. Lu, Q. Ma and H. Zhang, *Small Methods*, 2017, **1**, 1600030.
- [2] E. Sharmin and F. Zafar, *Metal-Organic Frameworks*, InTech, 2016, ch. Chapter 1, pp. 3–12.
- [3] C. Wiktor, M. Meledina, S. Turner, O. I. Lebedev and R. A. Fischer, *J. Mater. Chem. A Mater. Energy Sustain.*, 2017, **5**, 14969–14989.
- [4] S. Kitagawa and K. Uemura, *Chem. Soc. Rev.*, 2005, **34**, 109–119.
- [5] H. Furukawa, K. E. Cordova, M. O’Keeffe and O. M. Yaghi, *Science*, 2013, **341**, 974–974.
- [6] F.-X. Coudert, M. Jeffroy, A. H. Fuchs, A. Boutin and C. Mellot-Draznieks, *J. Am. Chem. Soc.*, 2008, **130**, 14294–14302.
- [7] A. P. Nelson, D. A. Parrish, L. R. Cambrea, L. C. Baldwin, N. J. Trivedi, K. L. Mulfort, O. K. Farha and J. T. Hupp, *Cryst. Growth Des.*, 2009, **9**, 4588–4591.
- [8] S. Turner, O. I. Lebedev, F. Schröder, D. Esken, R. A. Fischer and G. Van Tendeloo, *Chem. Mater.*, 2008, **20**, 5622–5627.
- [9] *Metal-organic frameworks : applications from catalysis to gas storage / edited by David Farrusseng.*, ed. D. D. Farrusseng, Wiley-VCH, Weinheim, 2011.
- [10] C. Healy, K. M. Patil, B. H. Wilson, L. Hermanspahn, N. C. Harvey-Reid, B. I. Howard, C. Kleinjan, J. Kolien, F. Payet, S. G. Telfer, P. E. Kruger and T. D. Bennett, *Coord. Chem. Rev.*, 2020, **419**, 213388.
- [11] S. L. James, *Chem. Soc. Rev.*, 2003, **32**, 276–288.
- [12] C. Wiktor, M. Meledina, S. Turner, O. I. Lebedev and R. A. Fischer, *J. Mater. Chem. A Mater. Energy Sustain.*, 2017, **5**, 14969–14989.
- [13] S. Yuan, L. Feng, K. Wang, J. Pang, M. Bosch, C. Lollar, Y. Sun, J. Qin, X. Yang, P. Zhang, Q. Wang, L. Zou, Y. Zhang, L. Zhang, Y. Fang, J. Li and H.-C. Zhou, *Adv. Mater.*, 2018, **30**, e1704303.
- [14] M. Ding, X. Cai and H.-L. Jiang, *Chem. Sci.*, 2019, **10**, 10209–10230.
- [15] N. C. Burtch, H. Jasuja and K. S. Walton, *Chem. Rev.*, 2014, **114**, 10575–10612.
- [16] O. Ugurlu, J. Haus, A. A. Gunawan, M. G. Thomas, S. Maheshwari, M. Tsapatsis and K. A. Mkhoyan, *Phys. Rev. B*, 2011, **83**, 113408.
- [17] S. Kretschmer, T. Lehnert, U. Kaiser and A. V. Krashennnikov, *Nano Letters*, 2020, **20**, 2865–2870.
- [18] B. Liang, D. Mücke, C. Leist, U. Kaiser, H. Qi, I. Cooley, E. Besley, Z. Wang, S. Park, R. Dong and X. Feng, *In Progress*, 2022.
- [19] P. G. Huray, *Maxwell’s Equations*, Wiley-IEEE Press, New York, NY, 2011.
- [20] S. T. Skowron, S. L. Roberts, A. N. Khlobystov and E. Besley, *Micron*, 2019, **120**, 96–103.
- [21] W. Kühlbrandt, *Science*, 2014, **343**, 1443–1444.
- [22] K. W. Urban, *Science*, 2008, **321**, 506–510.
- [23] C. Wiktor, S. Turner, D. Zacher, R. A. Fischer and G. V. Tendeloo, *Microporous and Mesoporous Materials*, 2012, **162**, 131–135.
- [24] N. I. Kato, *J. Electron Microsc. (Tokyo)*, 2004, **53**, 451–458.
- [25] R. Egerton, *Micron*, 2019, **119**, 72–87.
- [26] R. F. Egerton, P. Li and M. Malac, *Micron*, 2004, **35**, 399–409.
- [27] N. I. Kato, *J. Electron Microsc. (Tokyo)*, 2004, **53**, 451–458.

- [28] D. Nicholls, J. Lee, H. Amari, A. J. Stevens, B. L. Mehdi and N. D. Browning, *Nanoscale*, 2020, **12**, 21248–21254.
- [29] R. Egerton, P. Li and M. Malac, *Micron*, 2004, **35**, 399–409.
- [30] W. King, R. Benedek, K. Merkle and M. Meshii, *Ultramicroscopy*, 1987, **23**, 345–353.
- [31] T. W. Chamberlain, J. Biskupek, S. T. Skowron, P. A. Bayliss, E. Bichoutskaia, U. Kaiser and A. N. Khlobystov, *Small*, 2015, **11**, 622–629.
- [32] T. W. Chamberlain, J. Biskupek, S. T. Skowron, A. V. Markevich, S. Kurasch, O. Reimer, K. E. Walker, G. A. Rance, X. Feng, K. Müllen, A. Turchanin, M. A. Lebedeva, A. G. Majouga, V. G. Nenajdenko, U. Kaiser, E. Besley and A. N. Khlobystov, *ACS Nano*, 2017, **11**, 2509–2520.
- [33] J. C. Meyer, F. Eder, S. Kurasch, V. Skakalova, J. Kotakoski, H. J. Park, S. Roth, A. Chuvilin, S. Eyhusen, G. Benner, A. V. Krashennnikov and U. Kaiser, *Phys. Rev. Lett.*, 2012, **108**, 196102.
- [34] F. Neese, *Wiley Interdiscip. Rev. Comput. Mol. Sci.*, 2012, **2**, 73–78.
- [35] P. Hohenberg and W. Kohn, *Phys. Rev.*, 1964, **136**, B864–B871.
- [36] Y. Yang, M. N. Weaver and K. M. Merz, Jr, *J. Phys. Chem. A*, 2009, **113**, 9843–9851.
- [37] J.-H. Dou, L. Sun, Y. Ge, W. Li, C. H. Hendon, J. Li, S. Gul, J. Yano, E. A. Stach and M. Dincă, *J. Am. Chem. Soc.*, 2017, **139**, 13608–13611.
- [38] J. Park, A. C. Hinckley, Z. Huang, D. Feng, A. A. Yakovenko, M. Lee, S. Chen, X. Zou and Z. Bao, *J. Am. Chem. Soc.*, 2018, **140**, 14533–14537.
- [39] X. Huang, S. Zhang, L. Liu, L. Yu, G. Chen, W. Xu and D. Zhu, *Angew. Chem. Weinheim Bergstr. Ger.*, 2018, **130**, 152–156.

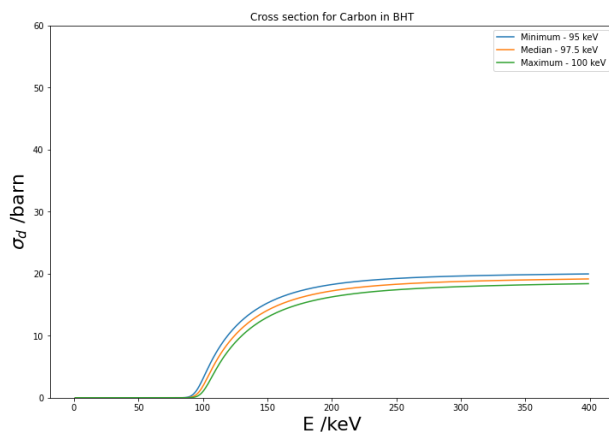
SUPPLEMENTARY INFORMATION

Table 5. The values used to calculate all total cross section values¹⁸

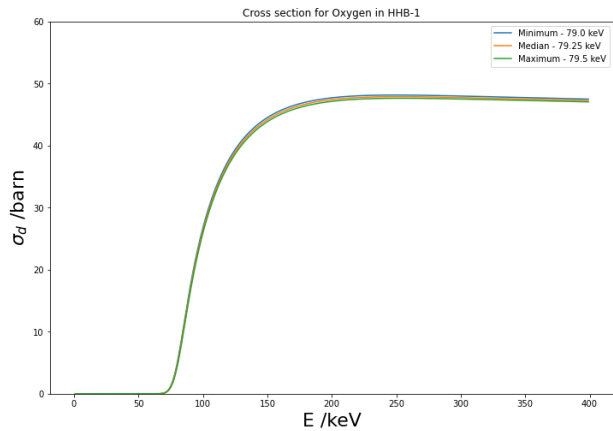
pka	Ejected Atom(S)	Atoms per Cu	Atoms per equivalent HHB-2 Cu	Atoms per Area	Range	Beam Energy (keV)	Transferred Energy (eV)
HHB-1							
C	C	2	6	0.123168057	Minimum	90	17.905
					Median	92.5	18.444
					Maximum	95	18.984
O	CO	2	6	0.123168057	Minimum	79	11.671
					Median	79.25	11.711
					Maximum	79.5	11.750
Cu	Cu	1	3	0.0615840287	Minimum	260	11.360
					Median	262.5	11.491
					Maximum	265	11.623
BHT							
C	C	2	6	0.0915339309	Minimum	95	18.984
					Median	97.5	19.527
					Maximum	100	20.073
S	S	2	6	0.0915339309	Minimum	164.5	13.095
					Median	164.75	13.118
					Maximum	165.0	13.141
Cu	Cu	1	3	0.045766965	Minimum	260	11.360
					Median	262.5	11.491
					Maximum	265	11.623



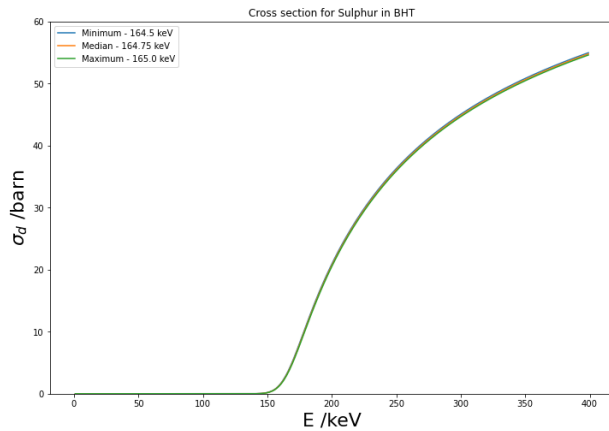
(a) HHB-1 Carbon Cross Section



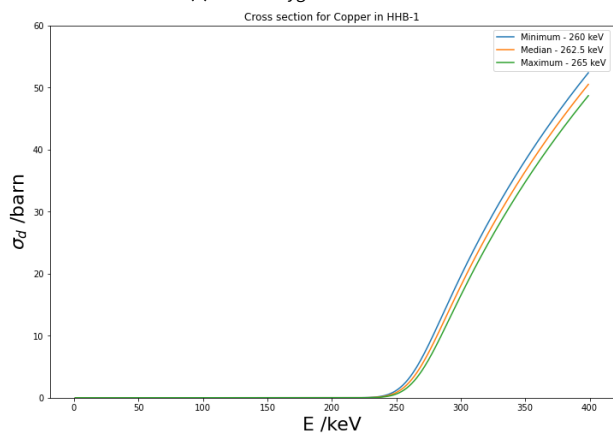
(b) BHT Carbon Cross Section



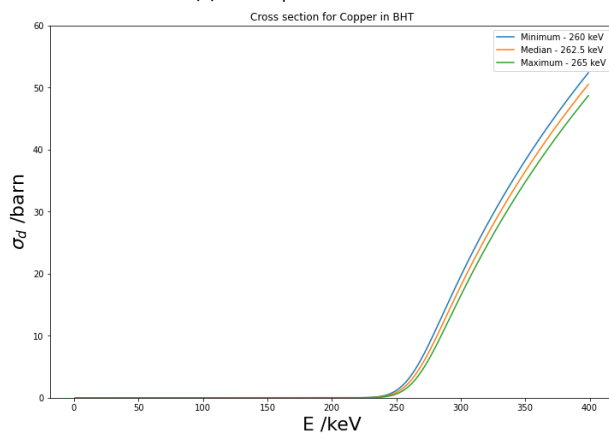
(c) HHB-1 Oxygen Cross Section



(d) BHT Sulphur Cross Section

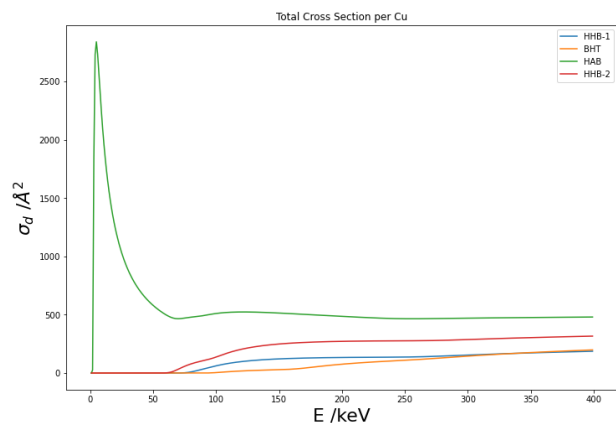


(e) HHB-1 Copper Cross Section

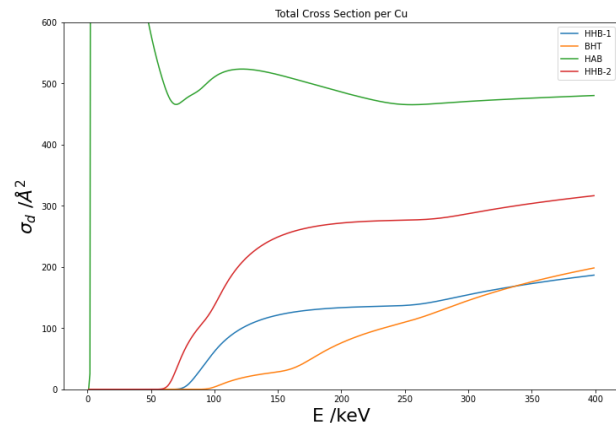


(f) BHT Copper Cross Section

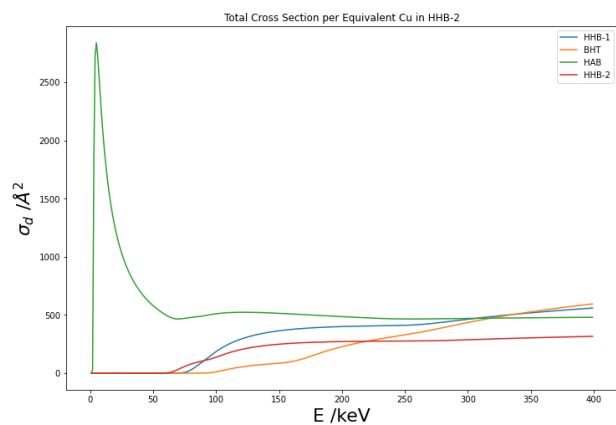
Figure 7. Cross Sections of atoms in HHB-1 and BHT



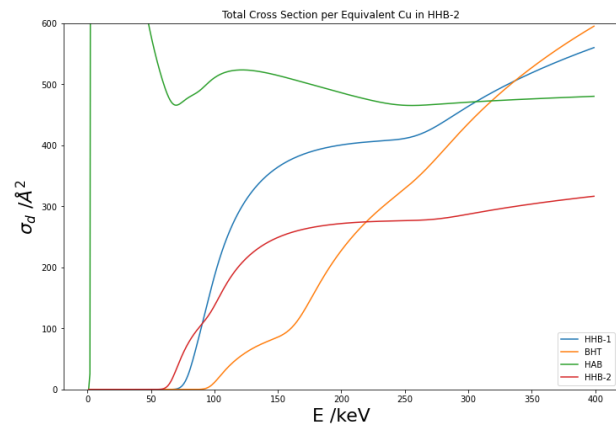
(a) Total Cross Section per Cu



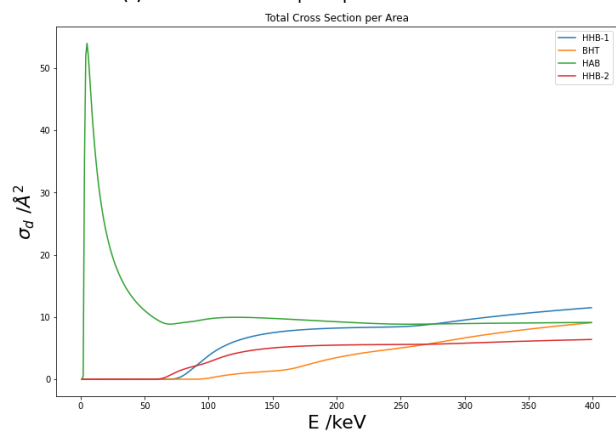
(b) Total Cross Section per Cu scaled



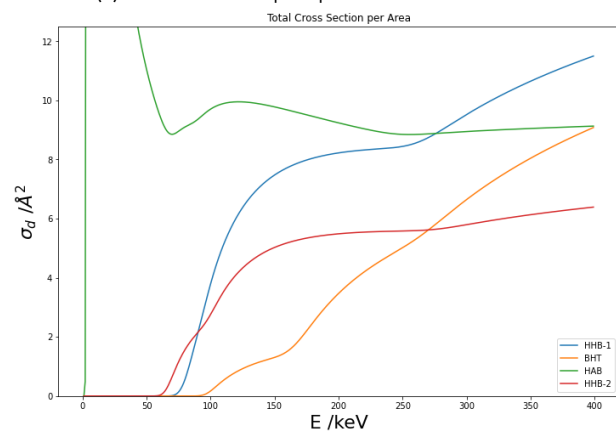
(c) Total Cross Section per Equivalent Cu in HHB-2



(d) Total Cross Section per Equivalent Cu in HHB-2 scaled



(e) Total Cross Section per Area



(f) Total Cross Section per Area scaled

Figure 8. Total Cross Section Approaches for the array of MOFs: HAB, HHB-2, HHB-1, and BHT